SILICON-INCORPORATED CARBON SPHERES AS ANODE MATERIAL FOR LITHIUM-ION BATTERIES

A Thesis

by

JIATANG CHEN

Submitted to the Office of Graduate and Professional Studies of
Texas A&M University
in partial fulfillment of the requirements for the degree of

MASTER OF SCIENCE

Chair of Committee,	Ying Li
Committee Members,	Hong Liang
	Xinghang Zhang
Head of Department,	Andreas A. Polycarpou

December 2015

Major Subject: Mechanical Engineering

ABSTRACT

In this study, a porous silicon-incorporated carbon material is studied as anode material in Lithium-ion batteries. This material is synthesized with carbonization, spray-pyrolysis and magnesiothermic reduction, from sucrose and silica as carbon and silicon precursors. Carbonization of sucrose was conducted in 0.125 M sulfuric acid with addition of colloidal silica at 90 ℃ for 48 hours. The C/SiO_2 spheres obtained from subsequent spray-pyrolysis were reduced by magnesium at 750 ℃ for 2 hours in a home-made Swagelok-type stainless steel reactor. The carbon was sacrificed to maintain the spherical structure of the composite during magnesiothermic reduction while silicon formed a highly porous sponge-like structure inside the spheres. C/Si (1:8) showed high recovery (85%) of specific capacity at the second cycle. However, the rapid capacity loss of porous silicon spheres was found to be caused by fracture the of thin silicon structure. Without the carbon shell, the debris dissolved into the electrolyte easily, leading to a lower availability of the silicon material.

ACKNOWLEDGEMENTS

I would like to acknowledge several people who contributed to this thesis and provided me guidance to achieve this.

First of all, I would like to express my deepest gratitude to my supervisor and committee chair, Dr. Li, for offering me the opportunity to work in the lab and guiding my research for the past two years. He is always supportive and encouraging me to be creative and has taught me the most important thing – critical thinking in research.

I would like to thank my committee members, Dr. Liang and Dr. Zhang. They both agreed to serve on my committee without hesitation, and also have provided guidance in my coursework at Texas A&M University.

Special thanks go to Dr. Kim and Dr. Polycarpou. Dr. Kim guided me from the beginning of the battery project. He assisted me in XRD, TEM characterization and discussed the problems with me during the project. Dr. Polycarpou provided the battery test equipment and glove box for my research. Without them, I could never have finished the project.

I also want to thank my labmates, Lianjun, Cunyu and Huilei for helping with my experiments as well as campus life.

Last but not least, I want to show my sincere appreciation to my family who are always physically, mentally and finically supportive when I am studying in the U.S.

NOMENCLATURE

LIB	Lithium-Ion Battery
CV	Cyclic Voltammetry
SEI	Solid-Electrolyte Interphase
CVD	Chemical Vapor Deposition
VLS	Vapor-Liquid-Solid
VS	Vapor-Solid
SFLS	Supercritical Fluid-Liquid-Solid
a-Li_xSi	Amorphous Li_xSi
P-milling	Discharge-Plasma-Assisted Milling
SICS	Silicon-incorporated Carbon Sphere
DI water	De-ionized water
LCVP	Laser Driven Chemical Vapor Pyrolysis
PCMs	Porous Carbon Microspheres
CB	Carbon Black
SAED	Selected Area Electron Diffraction
PAA	Polyacrylic Acid

TABLE OF CONTENTS

Page

LIST OF FIGURES

Page

LIST OF TABLES

Page

1 INTRODUCTION

In the past decade, the United State Environmental Protection Agency (EPA) has announced a series of measures against the severe threats raised by climate change. These include a more controllable and effective way of consuming fossil fuels. In the meanwhile, green and renewable energy sources such as solar, wind, thermal and hydroelectric energy should play a more important role in the global energy composition. Correspondingly, breakthrough in batteries has become more urgent than ever in history as they are the most convenient media to store and transfer electric energy for electronic device such as laptops and electric vehicles. Among current battery technologies, Lithium-ion batteries (LIBs) are promising due to its high volumetric and gravimetric energy. Lithium-ion battery is a member of the rechargeable battery family. In 1991, Sony and Asahi Kasei released the first commercial lithium-ion battery, which was used in mobile phones. The greatly increased energy density over conventional rechargeable batteries has enabled portable electronic device to shrive in outdoor environment.

1.1 Mechanism

In a typical Li-ion battery, charge and discharge are achieved by Li ions migrating through the electrolyte between the positive electrode (cathode) and negative electrode (anode), and electrons through the external circuit (see Figure 2). The cathode uses a lithium transition metal oxide while the anode uses a graphitic carbon. Both electrodes are able to reversibly insert and remove Li ions from their respective structures.[1] The liquid electrolytes in lithium-ion batteries consist of lithium salts, such

as $LiPF_6$, $LiBF_4$, $LiAsF_6$ or $LiClO_4$ in an organic solvent, such as ethylene carbonate, dimethyl carbonate, diethyl carbonate and so on.[2] On charging, Li ions deintercalated from the oxide compound are transported through the electrolyte and intercalated into the graphite layers. The reversed process happens on discharging. These two process are both benign and only cause a structural change of about 3% at the positive electrode and 10% at the negative electrode without any structural degradation. The reactions for graphite anode and $LiCoO_2$ cathode during charging are shown in Eq. (1) and (2) respectively.

$$Li^+ + e^- + 6C \Leftrightarrow LiC_6 \qquad (1)$$

$$LiCoO_2 \Leftrightarrow Li_{1-x}CoO_2 + xLi^+ + xe^- \qquad (2)$$

For graphite, Li ions are inserted in between graphene layers, each Li ion corresponding to six carbon atoms (see Figure 1), which results in a specific capacity of $C^S_{Graphite} = \frac{96485\ C/mol}{72\ g/mol} = 372\ \frac{mAh}{g}$ for graphite.

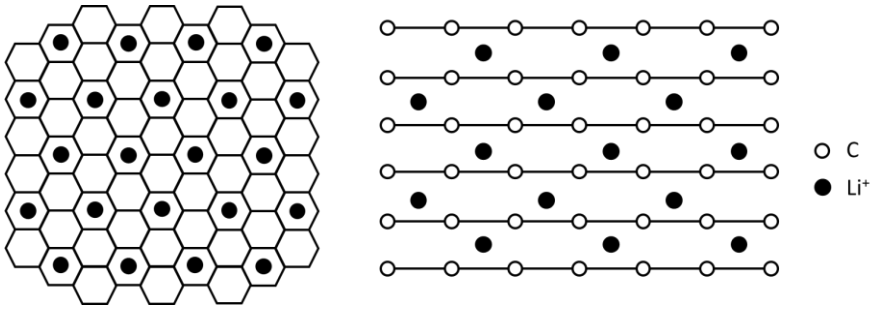

Figure 1. Intercalation of Li^+ between graphene planes of graphite.

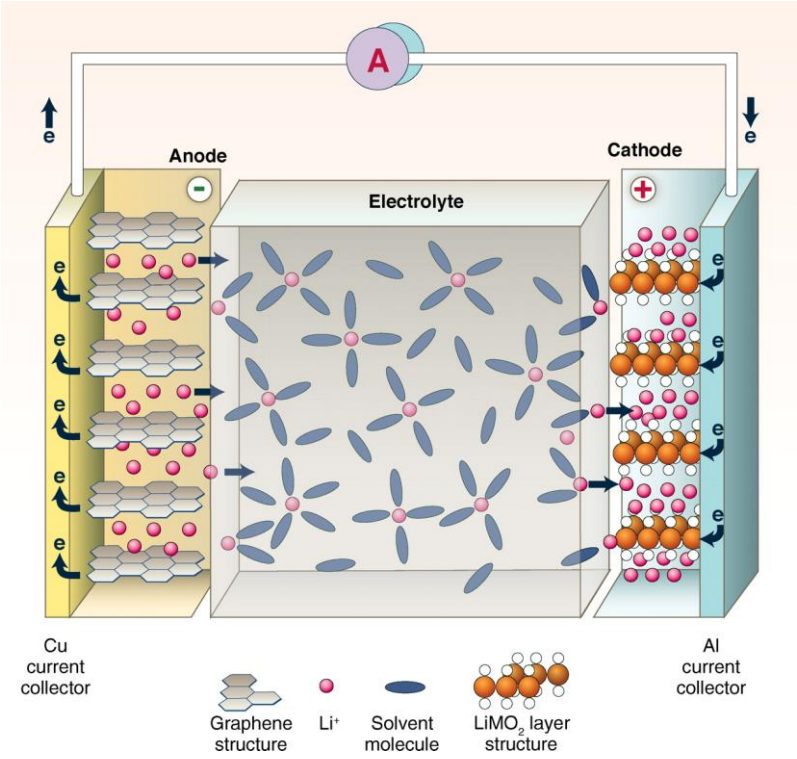

Figure 2. Schematic of a typical Li-ion battery showing the flow direction of Li^+ and electrons during charging process. Reprinted from ref. [1].

Si as one of the most abundant elements on earth has been studied in more advanced LIBs. Si-based LIB anode materials have received extensive attention because of the highest theoretical capacity ever known. The extremely high capacity is obtained from the Li_xSi alloy (x>1), i.e., much more electrons are provided per Si atom, compared with LiC_6 where six carbon atoms only provide one electron in a cycle. The alloy/de-alloy process is shown in Eq. (3),

$$xLi^+ + xe^- + Si \Leftrightarrow Li_xSi \qquad (3)$$

where x=1.71, 3.75, 4.20, 4.25, 4.40, corresponding to phases reported in literature[3]: $Li_{12}Si_7$, $Li_{15}Si_4$, $Li_{21}Si_5$, $Li_{17}Si_4$, $Li_{22}Si_5$. The corresponding specific capacities for these Li-Si phases are listed in Table 1.

Table 1. Theoretical specific capacities of Li-Si alloys.

Li-Si alloy	Theoretical Specific Capacity ($mAhg^{-1}$)
$Li_{12}Si_7$	1636
$Li_{15}Si_4$	3579
$Li_{21}Si_5$	4008
$Li_{17}Si_4$	4056
$Li_{22}Si_5$	4199

Theoretical calculation shows that Si has a specific capacity ten times higher than that of graphite, which is the most popular Li-ion battery anode material in the market.

1.2 Challenges for Li-ion batteries

The main constrain for current commercial Li-ion batteries is the low specific capacity, accompanying large volume and heavy weight. While the alloying structure of Si-based anodes manages to provide an extremely high capacity to solve the problem, it also brings some amplified structural issue to researchers. The volume change during alloying/de-alloying processes of Si can reach 300-400%, causing enormous mechanical

stress, structural pulverization and disconnection from the current collector, resulting in loss of capacity and poor Coulombic efficiency upon cycling.[4, 5] When pure Si particles are used as anode materials, the aggregation also leads to severe capacity loss and poor cycle performance due to the dropping of active sites, poor electron transport and slow Li ion diffusion. [6-10]

Another challenge for Li-ion batteries is the requirement of a stable solid-electrolyte interphase (SEI) to maintain high Coulombic efficiency and thus a long cycle life. During the cycling, Electrolyte oxidized at the positive electrode can migrate to the negative electrode and gets reduced to form some reaction product film, i.e., SEI. This passive SEI layer is inactive and protecting the rest of Si material. However, when cracks and pulverization occur at the electrodes, the SEI will be destroyed structurally expose the new Si surface to the electrolyte. A thicker SEI is formed consequently with higher electronic resistivity, slower Li ion diffusion and larger irreversible capacity. [11, 12] Note that another reason for the dissolution of SEI is using the battery at high temperature, which is not concerned in this study. More detailed Li-ion anode ageing mechanisms have already been summarized in literature by Vetter et al.[13]

Based on upon-mentioned discussions, anode material design is aimed at solving battery capacity and life problems. In other words, a well-designed Si-based material should have good properties in the following aspects: a) accommodation for volume change during lithiation/de-lithiation; b) stability of SEI to maintain high Coulombic efficiency; c) Li-ion diffusion to enable fully usage of the material; d) contact with current collector and impedance; and e) cost and safety issues.

2 LITERATURE REVIEW

Silicon as electrode material has been studied by many research groups for its high theoretical specific capacity (4200 $mAhg^{-1}$) compared to graphite used in conventional batteries (372 $mAhg^{-1}$). These silicon-based materials can be summarized into three catalogs: 1D nanowires (NWs) and nanotubes (NTs), 2D thin films and 3D nanocomposites. These structures are designed for the same purpose – to constrain or accommodate the volume expansion during the lithiation process of silicon, and create a stable solid-electrolyte interphase (SEI).

2.1 1D nanowires (NWs) and nanotubes (NTs)

Silicon-based nanowires and nanotubes used in electrode materials are usually around the size of 100 nm in diameter.[14-18] Usually two ways are used to arrange the 1D structures on current collectors: crossing network[19] and vertical array[18] (see Figure 3). Both configurations provide empty space between NWs/NTs for volume expansion. With excellent strain and volume accommodation, the mechanical properties also enables the electrode to maintain its structure after many charge/discharge cycles and contribute to long life. For vertical arrays, Si NWs/NTs are usually grown directly on the current collector, thus possess excellent contact with good conductivity, which is also an important factor affecting electrochemical performance. In addition, the elongated structure allows for larger specific area for lithiation and de-lithiation reaction without increasing bulk mass. Compared with nanowires, nanotubes have another advantage that allows inward expansion of Si, mitigating the damage of SEI on the cylinder outer wall.

C/Si and Si/C core-shell nanowires are also reported in literature to have better cycle performance than normal Si nanowires.[14, 16] Carbon nanofibers (CNFs) coated with silicon was reported by Cui et al. using SiH_4 CVD. In this C/Si core-shell structure, the carbon core acts as an efficient electron conducting pathway as well as the mechanical support due to a small structural deformation under lithiation/de-lithiation. Bogart et al. reported the Si/C core-shell nanowires synthesized by supercritical fluid-liquid-solid (SFLS) and pyrolysis with polyphenylsilane. The improvement is explained the carbon skin covering Si nanowires can speed up the lithiation of Si by one order while preventing the crystalline structure from converting to amorphous Li_xSi (a-Li_xSi).

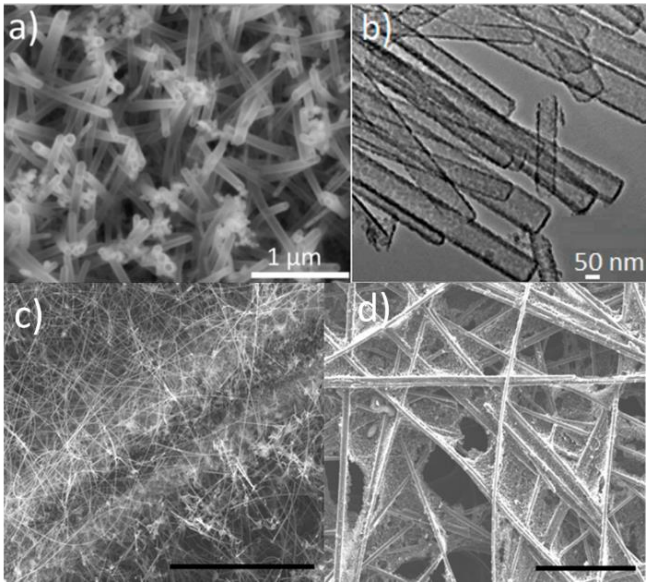

Figure 3. Arrangement of Si nanowires/nanotubes: a) and b) NWs/NTs array; c) and d) NWs/NTs tissue-like network. Reprinted from ref. [18] and [19].

2.2 2D thin films

Pure Si thin films are normally vulnerable to fracture and pulverization caused by the large volume change during lithium insertion/extraction. As a result, the active material can easily lose contact with the current collector, which directly leads to impedance rise as well as capacity loss. Pure Si thin films reported in literature[20, 21] have a limitation on the thickness. When the thickness is about 250 nm, the electrode material exhibit high capacity and cycle performance. However, when the thickness is increased to 1 μm or more, the capacity drops rapidly after very few cycles. The main reason is that the large bulk cannot accommodate the substantial volume change and causes structural failure under lithiation/de-lithiation.

CNT-Si films (see Figure 4) reported by Cui et al. have achieved significant cycle performance improvement by introducing a structure similar to the steel bar reinforced concrete, where CNTs act as mechanical support and electrical conductor.[22] Compared with traditional Si film, the concrete-like film is able to bend under repeated Si expansion even with a thickness of 4 μm.

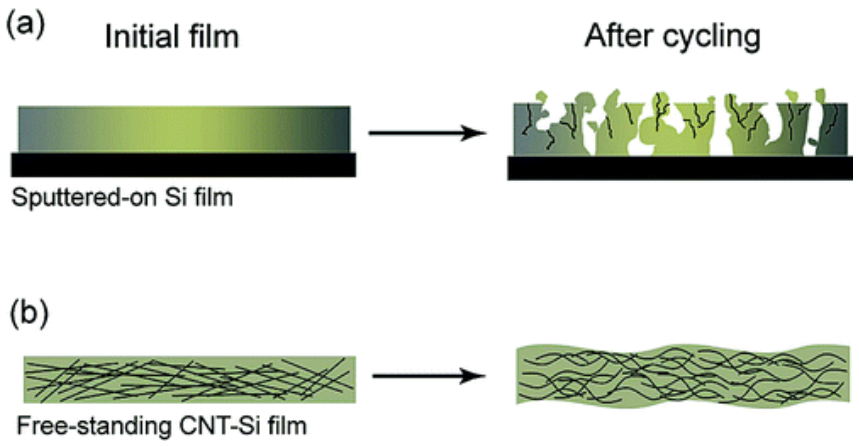

Figure 4. a) Sputtered-on Si film pulverizes after Li^+ cycling. b) CNT-Si films "ripple up" to relax the large strain during Li^+ cycling. Reprinted from ref. [22].

2.3 3D nanocomposites

3D structures discussed in this work include nanoparticles (see Figure 5)[23], hollow particles (see Figure 6)[24] and porous particles[8]. For solid nanoparticles, the accommodation of volume change is achieved by dispersing nanosized Si particles and introducing graphene, CNTs or carbon coating, which can act as mechanical support and conducting network. Hollow and porous particles as more exquisite structures have been reported. Compared with solid particles, hollow and porous possess some advantages: 1) larger specific area and thus more effective for lithiation reaction; 2) large void space inside the particle to allow volume expansion in every direction; and 3) shorter diffusion distance for electrons and lithium ions. [25]

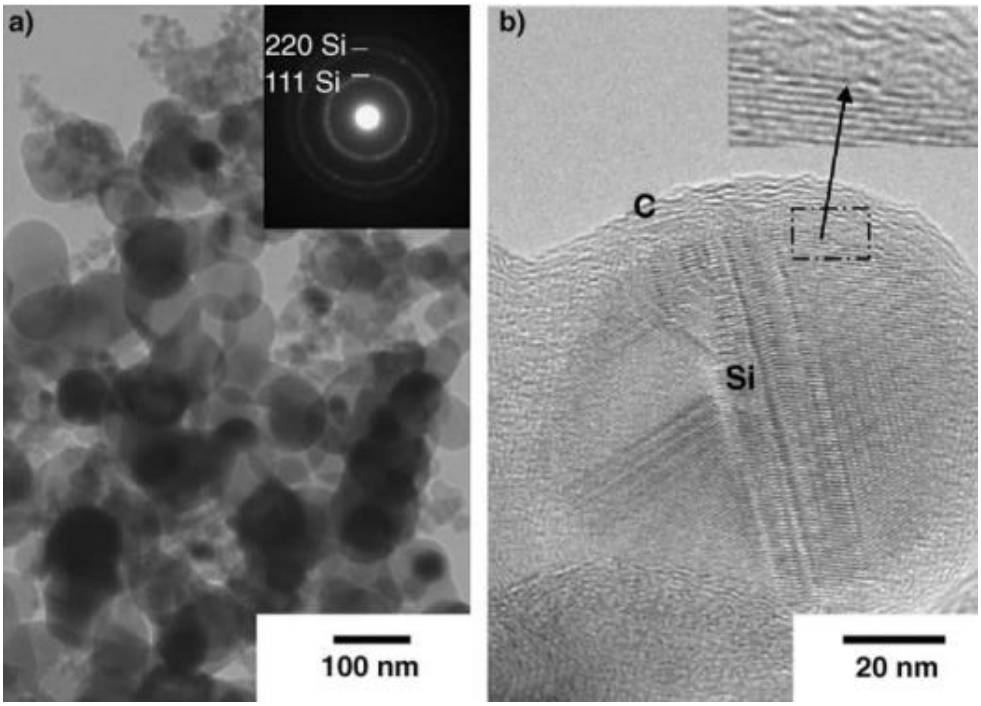

Figure 5. TEM images of spheroidal carbon-coated Si nanocomposites produced by spray pyrolysis in air: a) low-magnification image of a sample produced at 4008C, with the indexed diffraction pattern (inset) confirming the presence of Si nanoparticles; b)high-resolution image showing the carbon-coated Si nanocomposite, with the inset showing the interface between a crystalline Si particle and the pyrolyzed carbon coating layer (ca. 10 nm thickness). Reprinted from ref. [23].

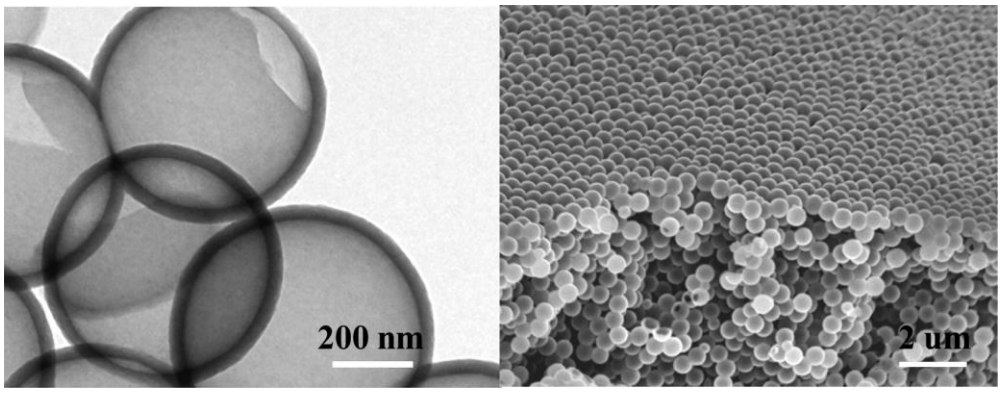

Figure 6. TEM and SEM images of interconnected hollow Si spheres (R_{in} ~ 175 nm, R_{out} ~ 200 nm). Reprinted from ref. [24].

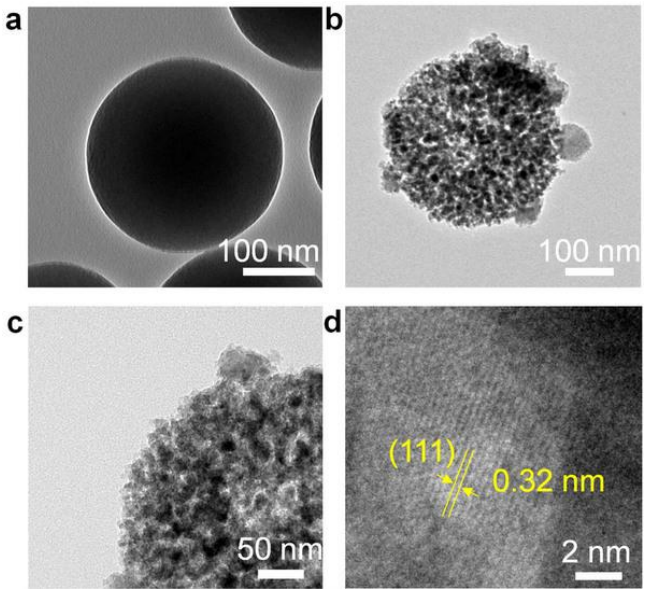

Figure 7. TEM images of (a) monodisperse solid silica spheres and (b–d) monodisperse porous silicon spheres, respectively. Reprinted from ref. [8].

Some typical Si-based electrode materials, their properties and cycle performance are summarized in Table 2. For most Si-based material, the cycle life is not long enough for commercial use. In addition, when pure silicon or silane gas is used as silicon source, the cost is usually very high.

Table 2. Si-based materials and their performance in literature. C rate: 1 C means to charge or discharge the battery in 1 hour, 0.1 C corresponds to 10 hours. Size explanation: ID - inner diameter, OD - outer diameter.

	Structure	Size (nm)	Initial Capacity/End Capacity ($mAhg^{-1}$) Cycles, C Rate	Synthesis Method	Reference
1D	Si NWs	OD: 89	4277/3500 20 cycles, 0.2C	VLS or VS	[15]
	C/Si core-shell NWs	Si shell thickness: 50	-/2000 30 cycles, 0.2C	CVD	[16]
	Si/C core-shell NWs	OD: ~100	-/2000 100 cycles, 0.1C	SFLS	[14]
	Si NTs	ID: 30 OD: 60 - 110	-/2000 50 cycles, 0.2C	Template, CVD	[18]
	Porous doped Si NWs	Pore D: 8	-/2000 250 cycles, 0.5C	HF etching	[17]
2D	Si thin film	Thickness: 250	4100/3500 30 cycles, 0.4C	Magnetron sputtering	[20]
	Si thin film	Thickness: 275	2463/1316 500 cycles, 0.5C	Magnetron sputtering	[21]
	CNT-Si film	Thickness: 4000	2083/1711 50 cycles, 0.1C	CVD	[22]
3D	Si/Graphene	Si: 100 Graphene: 10	-/866 200 cycles, $0.4mA/cm^2$	P-milling	[26]
	C coated Si spheres	OD: 100	2600/1489 20 cycles, 100mA/g	Spray-pyrolysis	[23]
	Si hollow spheres	ID: 175 OD: 200	3544/2725 700 cycles, 0.1C	CVD, HF etching	[24]
	Porous Si/CNTs	OD: 200	-/1500 500 cycles, 0.5C	Magnesiothermic reduction	[8]

2.4 Porous carbon materials

Porous carbon spheres encapsulating metals/metal oxides have been reported with synthesizing methods including spray-pyrolysis[23, 27], electrospraying[28], lazer driven chemical vapor pyrolysis(LCVP)[29] and industrial organic templating[30]. Normally, carbon is produced from carbonization or thermal decomposition of organic chemicals such as sucrose, ethylene and polyvinyl chloride. The hard templates or soft templates are then dealt with in two possible ways: 1) removed with strong base or acid to form the void space in carbon spheres; 2) altered to form some valuable component in carbon spheres. Porous carbon spheres after calcination are reported to have good mechanical strength as well as high surface area, making this material a good candidate as substrate.

2.5 Summary of literature review

The main constrain for current commercial Li-ion batteries is the low specific capacity, accompanying large volume and heavy weight. While the alloying structure of Si-based anodes manages to provide an extremely high capacity to solve the problem, it also brings some amplified structural issue to researchers. The volume change during alloying/de-alloying processes of Si can reach 300-400%, causing enormous mechanical stress, structural pulverization and disconnection from the current collector, resulting in loss of capacity and poor Coulombic efficiency upon cycling.[4, 5] When pure Si particles are used as anode materials, the aggregation also leads to severe capacity loss and poor cycle performance due to difficulty of releasing stress, poor electron transport and slow Li ion diffusion. [6-9]

Another challenge for Li-ion batteries is the requirement of a stable solid-electrolyte interphase (SEI) to maintain high Coulombic efficiency and thus a long cycle life. During the cycling, Electrolyte oxidized at the positive electrode can migrate to the negative electrode and gets reduced to form some reaction product film, i.e., SEI. This passive SEI layer is inactive and protecting the rest of Si material. However, when cracks and pulverization occur at the electrodes, the SEI will be destroyed structurally and expose the new Si surface to the electrolyte. A thicker SEI is formed consequently with higher electronic resistivity, slower Li ion diffusion and larger irreversible capacity.[11] Note that another reason for the dissolution of SEI is using the battery at high temperature, which is not concerned in this study. More detailed Li-ion anode ageing mechanisms have already been summarized in literature by Vetter et al.[13]

Based on upon-mentioned discussions, anode material design is aimed at solving battery capacity and life problems. In other words, a well-designed Si-based material should have good properties in the following aspects: a) accommodation for volume change during lithiation/de-lithiation; b) stability of SEI to maintain high Coulombic efficiency; c) Li-ion diffusion to enable fully usage of the material; d) contact with current collector and impedance; and e) cost and safety issues.

3 OBJECTIVE, MATERIAL DESIGN AND SYNTHESIS

3.1 Objective

Silicon anode materials usually shows a specific capacity higher than 3000 mAh/g in the first cycle and drops to lower than 2000 mAh/g in the second cycle. The subsequent reversible capacity is what truly matters. For the material proposed in this study, a specific capacity of higher than 1000 mAh/g with good stability is expected for the silicon composition after 100 cycles. This will be four times higher than commercial graphite-Lithium Cobalt oxide batteries. In current electric vehicles, the battery pack can contain more than 7000 cells (18650 type) to get energy as high as 60 kWh or a travel distance of 300 miles for one single charge. The total weight of the cells is higher than 300 kg. With a specific capacity four times higher, the weight of the battery pack can be reduced to less than 100 kg. In other word, with the same battery weight, a single charge can support more than 1000 miles.

From the perspective of material, this study is also aimed at investigating the factors affecting the performance of silicon reduced from silica by examining the proposed structure in the following.

3.2 Material design

In this study, a double porous structure -- porous Si incorporated into carbon spheres (see Figure 8), is proposed to meet the aforementioned principles. The carbon (300-3000 nm) covering silicon acts as a conducting layer and mechanical substrate to keep the incorporated silicon works effectively during lithiation and de-lithiation. The silicon itself also possess the porous structure to accommodate volume change in

cycling. This porous structure is generated from the removal of MgO, which ideally occupies 65% of the total volume. The conductivity is also guaranteed since the silicon is sitting in cages. Compared with direct use of silicon in literature, this material uses silica as silicon precursor and sucrose as carbon precursor, both cost-effective and abundant on earth.

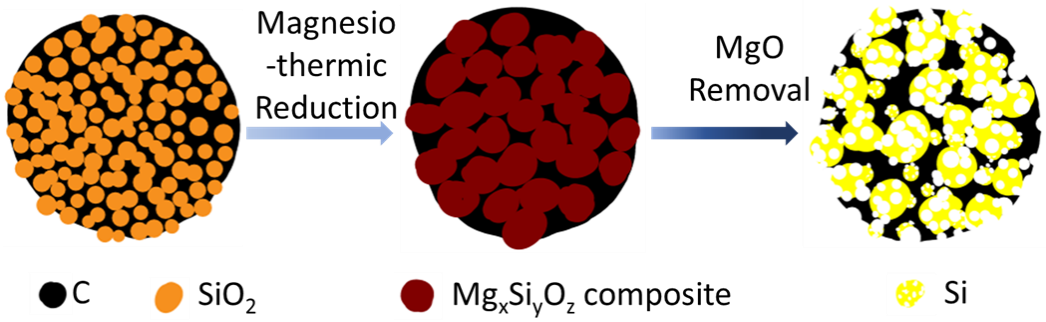

Figure 8. Porous structure generated from carbonization and magnesiothermic reduction.

3.3 Material synthesis

Silicon-incorporated Carbon Spheres are synthesized through three main steps: carbonization of sucrose, spray-pyrolysis and magnesiothermic reduction.

3.3.1 Carbonization of sucrose

Sucrose ($C_{12}H_{22}O_{11}$) is used as the precursor of carbon. The carbonization process is conducted in a round bottom flask in silicone oil bath under stirring for 36 hours till the color of the solution become dark brown (see Figure 9). Colloidal silica (SNOWTEX, ST-OL) with the size of 50 nm is added into the round bottom flask with ratios of $C:SiO_2$ = 1:2, 1:5 and 1:8 by weight, the corresponding final products are

labeled as C/Si (1:2), C/Si (1:5) and C/Si (1:8). Sulfuric acid (BDH) is added to the suspension with the concentration of 0.125 M. The oil temperature is maintained at 90 ℃. Eq. (4) shows the overall reaction of the carbonization process.

$$C_{12}H_{22}O_{11} + H_2SO_4 \rightarrow 12C + 11H_2O + H_2SO_4 \qquad (4)$$

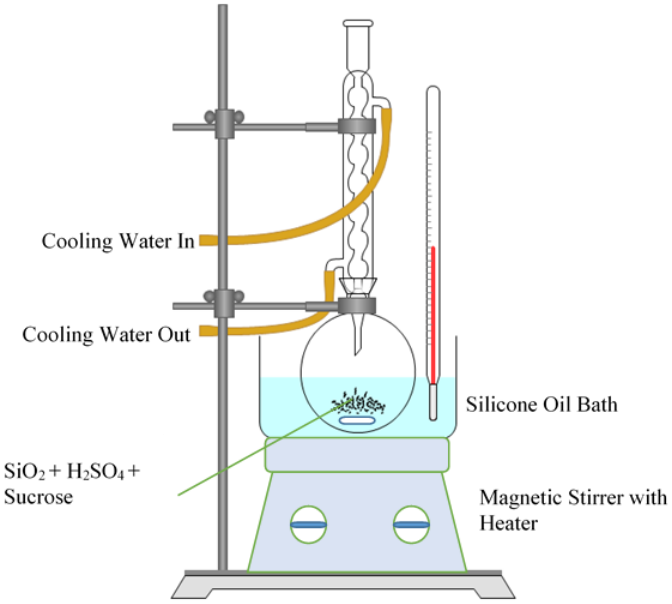

Figure 9. Schematic of carbonization of Sucrose.

3.3.2 Spray-pyrolysis

Compressed air is used as feeding gas to spray out the suspension through a nebulizer after carbonization process (see Figure 10). The tube furnace is set at 600 ℃. A collector embedded with a glass fiber filter is installed after the quartz tube to collect the powder product. The product is calcined at 750 ℃ in Argon for 2 hours to remove impurities and ensure complete carbonization.

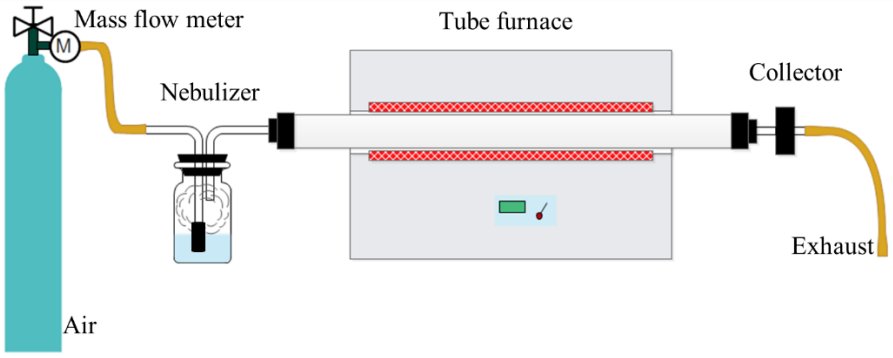

Figure 10. Schematic of the synthesis of sphere particles with spray-pyrolysis method.

3.3.3 Magnesiothermic reduction

A home-made Swagelok-type stainless steel reactor is used for the magnesiothermic reduction of silica (see Figure 11). C/SiO_2 spheres obtained from spray-pyrolysis is mixed with magnesium powder (Alfa, 325 mesh) with the molar ratio of Si:Mg = 1:2 and then sealed inside the reactor. This process needs to be done inside the glove box filled with argon to avoid contact of magnesium with air. The reactor is then inserted into the quartz tube. Ar is again used as the protecting gas between the reactor and quartz tube. Purging is needed before the tube furnace is heated up. The temperature is maintained at 750 ℃ for two hours and then cooled down naturally. The main magnesiothermic reaction is shown in Eq. (5) with possible coupled reactions shown in Eq. (6) and (7). The product containing impurities (MgO, Mg_2Si) is put into 2M HCl solution at 60 ℃ for 2 hours and then washed with DI water. Leaching reactions are shown in Eq. (8) and (9). Note that the silane (SiH_4) generated from reaction (9) will ignite and cause small explosions when exposed to air as shown in Eq. (10). Therefore, the leaching process has to be operated with the fume hood.

$$2Mg(s) + SiO_2(s) \rightarrow 2MgO(s) + Si(\text{s}) \quad (5)$$

$$4Mg(s) + SiO_2(s) \rightarrow 2MgO(s) + Mg_2Si(\text{s}) \quad (6)$$

$$Mg_2Si(\text{s}) + SiO_2(s) \rightarrow 2MgO(s) + 2Si(s) \quad (7)$$

$$MgO(s) + 2HCl(l) \rightarrow MgCl_2(l) + H_2O(l) \quad (8)$$

$$Mg_2Si(s) + 4HCl(l) \rightarrow SiH_4(g) + 2MgCl_2(l) \quad (9)$$

$$SiH_4(g) + 2O_2(g) \rightarrow SiO_2(s) + 2H_2O(g) \quad (10)$$

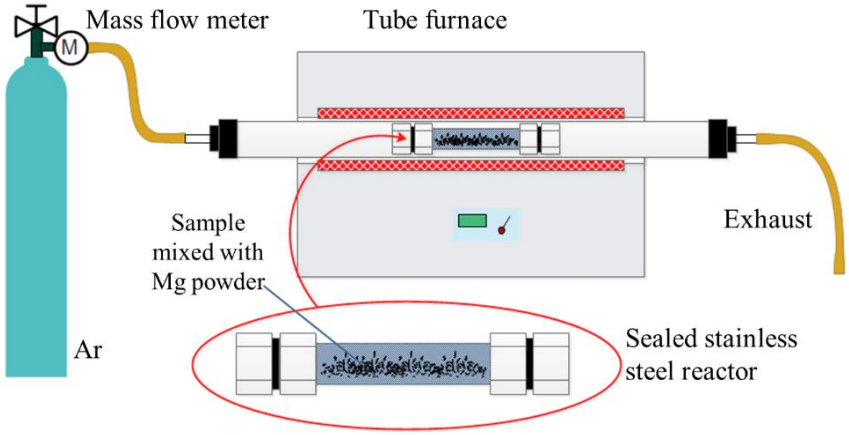

Figure 11. Magnesiothermic reduction of Silica to Silicon

3.4 Material characterization

The morphology and composition of materials used in this study were characterized by the following techniques. Characterization results are analyzed in Results and Discussion section.

3.4.1 Scanning electron microscopy (SEM)

The morphology of samples before and after magnesiothermic reduction was characterized by JEOL JSM-7500F field emission SEM.

3.4.2 Transmission electron microscopy (TEM)

An FEI TECNAI G2 F20 ST FE-TEM was used to characterize the nanostructure of the samples. Selected area electron diffraction (SAED) was used to identify the crystal structure.

3.4.3 X-ray diffraction (XRD)

Crystal structure was obtained by XRD from 10 to 90 degree. The peaks were compared to and identified with literature.

4 BATTERY PERFORMANCE TESTS

4.1 Anode preparation

The as-prepared active materials are mixed with the binder PAA (Sigma-Aldrich, 35%)[31] in the ratio of SICS:PAA:CB=70:15:15 in a mortar. The slurry is then coated on a copper foil with a doctor blade and then dried in a vacuum oven at 100 ℃ overnight. Anode disks are then punched from the copper foil and weighed separately. Figure 12 shows the preparation process of anodes.

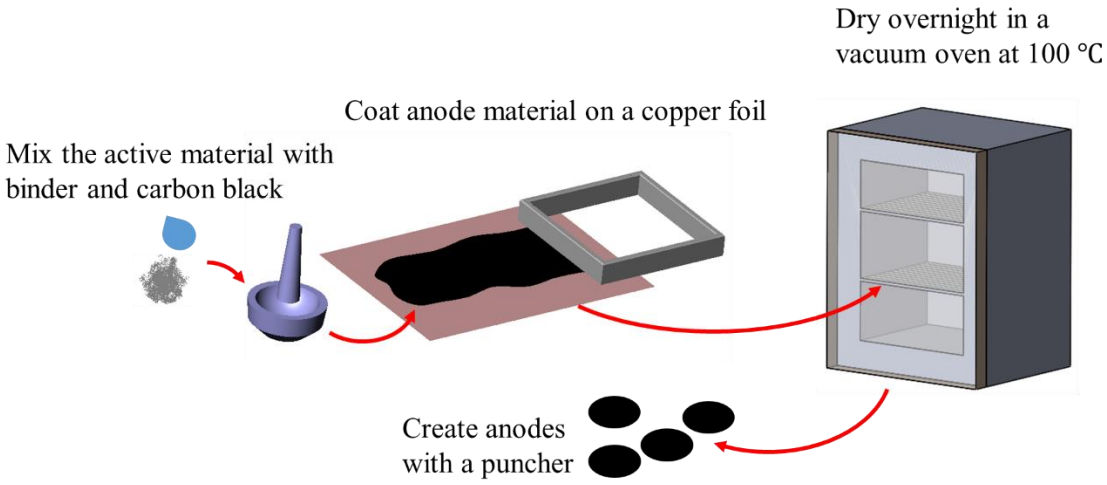

Figure 12. Schematic of anode preparation.

4.2 Battery cell assembly

The assembly of the half-cell is conducted inside the argon glove box. The solid components include the lid, bottom, spacer, spring, separator, electrolyte, cathode and anode, as shown in Figure 13. Metallic lithium foil is used as cathode to provide "infinite" Li ions, thus to exclude the limiting effect of cathode.

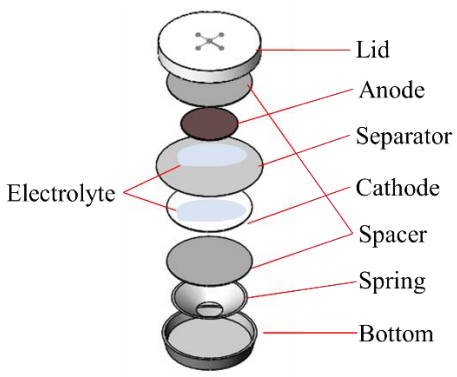

Figure 13. Basic components of a coin cell battery.

4.3 Galvanostatic charge–discharge (GCD) test

A CHI electrochemical station was used to run the cycling tests. The cycling was carried out by charging/discharging at set current rate (or C-rate). The data obtained included the change of specific capacity, reversibility, cycle life of the batteries.

4.4 Cyclic voltammetry (CV) test

CV test generated the voltage-current diagram by applying potential scans to the working electrode. The peaks of CV curves indicated the chemical reaction during charging and discharging.

5 RESULTS AND DISCUSSION

The morphology of samples before and after magnesiothermic reduction is shown in Figure 14. Pure silica particles (15-20 nm) formed a continuous and highly porous structure after reduction (see Figure 14a right). The large bulk size might result from sintering effect. The channel size ranges from 100 nm to 200 nm in diameter, which is about ten times the size of the original particles. This sponge-like structure is formed from the removal of MgO. In other words, Mg was able to diffuse into SiO_2 thoroughly and uniformly, reconstructing a completely new structure during reaction at 750 ℃. Figure 15 shows the TEM images of C/Si (1:8). The (111) (220) and (311) planes of silicon can be seen from the selected area electron diffraction (SAED) pattern. Figure 14b and 14c show the C/SiO_2 ($C:SiO_2$ = 1:5 and 1:8) structure after spray-pyrolysis (left) and magnesiothermic reduction (right), respectively. From the left image, the C/SiO_2 spheres look like a conglomeration of SiO_2 particles. This is due to the low content of carbon, which was acting as a “glue” rather than a “shell”. From Figure 14b and 14c, the reduced C/SiO_2 showed a similar inner structure to reduced SiO_2, suggesting the magnesium vapor was able to infiltrate into the C/SiO_2 spheres. At higher content of SiO_2, the “sponge” structure was more porous due to more removed volume of MgO. Note that the inner structure of reduced C/SiO_2 was similar to reduced SiO_2, the spherical shape of about half of the sample, however, was maintained due to the addition of carbon composition. In addition, SiC as an impurity also existed in the sample according to XRD characterization (see Figure 16).

Pure silicon anode material (Si powder, 30 nm) showed an initial capacity (3300 mAh/g) (see Figure17) close to theoretic value (3579 mAh/g), which is attributed to the nanosized structure. However, the capacity drops significantly and rapidly after the first two cycles. After 100 cycles, the specific capacity has dropped to 188 mAh/g, less than 1/10 of the initial value. This is due to the great stress generated from lithiation/de-lithiation process. The stress between particles disintegrated the structure connected by the binder, although the individual nanoparticles could maintain intact under expansion and shrinkage.

C/SiO_2 (1:2) showed lowest specific capacity among all samples tested (see Figure 19). When the charging/discharging rate was higher than 100 mA/g, the specific capacity was lower than 100 mAh/g. This is probably because the carbon spheres are fully occupied, making lithium ions hard to diffuse into the microspheres.

PCMs obtained by soaking C/SiO_2 (1:2) into 10% HF solution for 24 hours showed a specific capacity much higher than commercial carbon materials and comparable to those reported in literature[27]. At a charging/discharging rate of 100 mA/g, PCMs gave a capacity higher than 600 mAh/g, about twice the theoretic capacity of graphite. This means the mesoporous size (50 nm) is working well for lithium ion diffusion, and the conductivity maintains well. However, from Figure 18, the capacity dropped from 1466 mAh/g to 607 mAh/g in just one cycle at 100 mA/g. The large irreversible capacity indicates that the high initial capacity might be attributed to the high specific surface area in the porous structure, which profoundly enhanced the

adsorption of Li ions. This part of Li ions nevertheless did not participate in subsequent cycling.

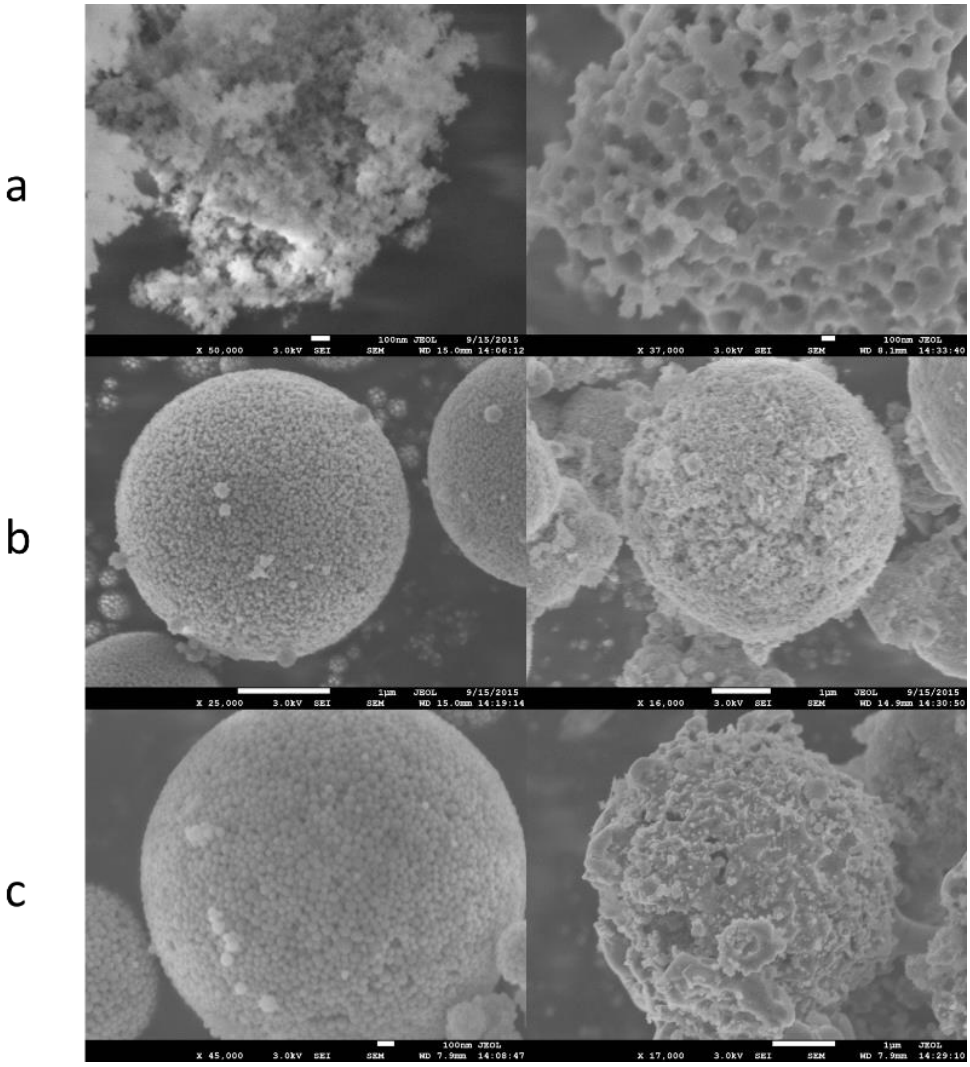

Figure 14. a) SEM image of reduced SiO_2; b) C/SiO_2 (1:5) and reduced product; c) C/SiO_2 (1:8) and reduced product. The images before reduction are on the left and after reduction on the right.

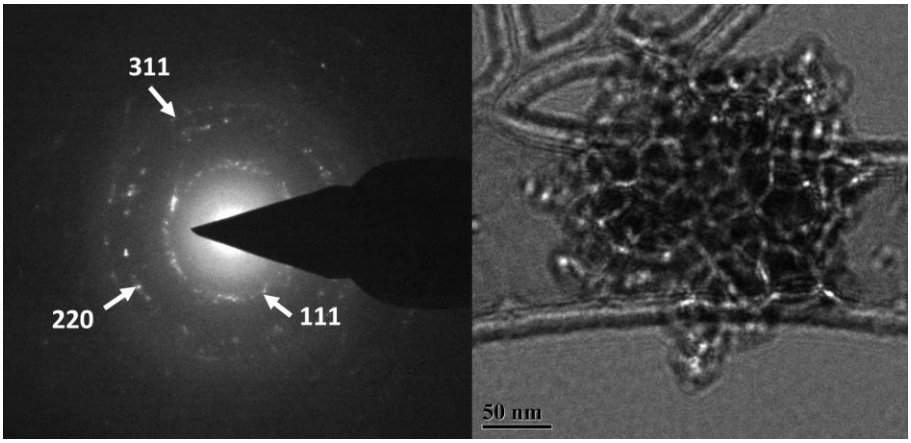

Figure 15. TEM image and SAED pattern of C/Si (1:8) showing Si crystal structure.

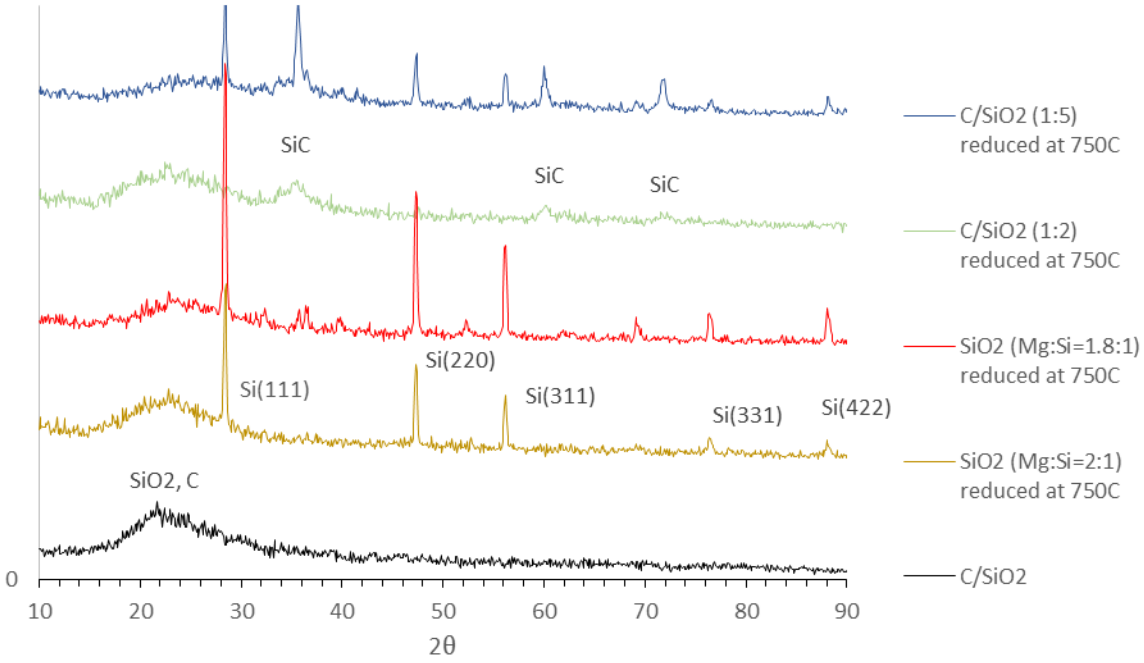

Figure 16. XRD patterns of C/SiO_2 spheres, reduced SiO_2, and reduced C/SiO_2 spheres with ratios of C:SiO_2 = 1:2 and 1:5.

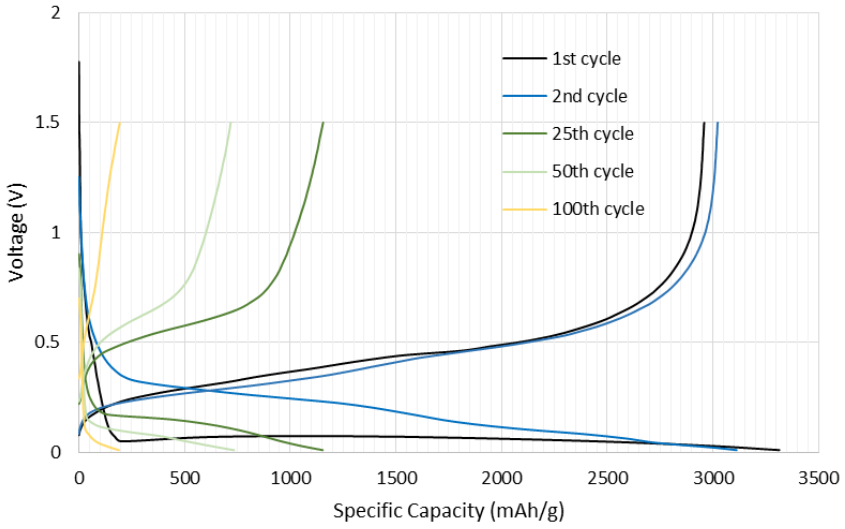

Figure 17. Cycle performance of Si (30 nm) nanoparticles as anode material at a charging/discharging current rate of 3000 mA/g.

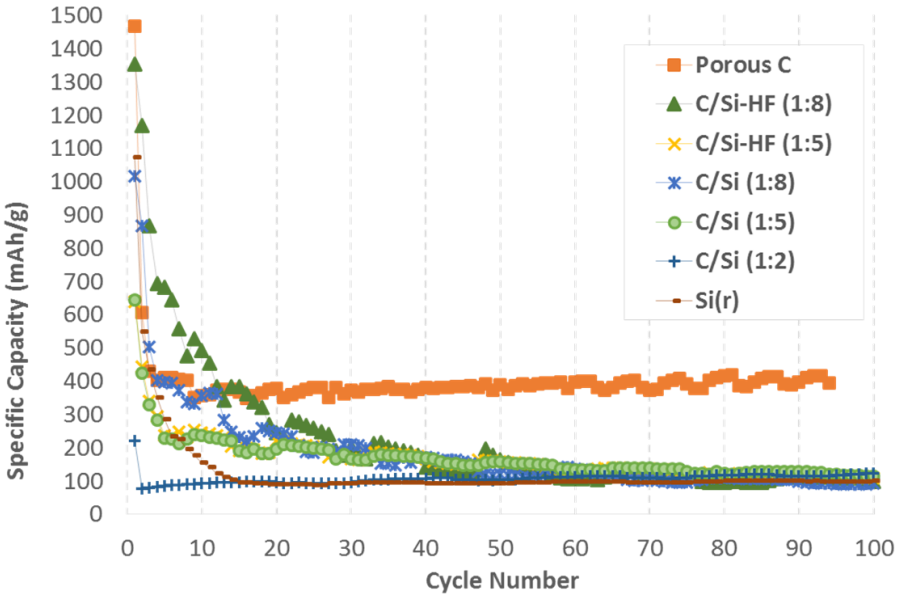

Figure 18. Cycle performance of reduced silica Si(r), carbon spheres, reduced C/SiO_2 (1:2, 1:5 and 1:8), and samples treated with sonication in 10% hydrofluoric acid for 5 min. All tests were performed at a charging/discharging current rate of 100 mA/g for the first two cycles and 200 mA/g for the rest.

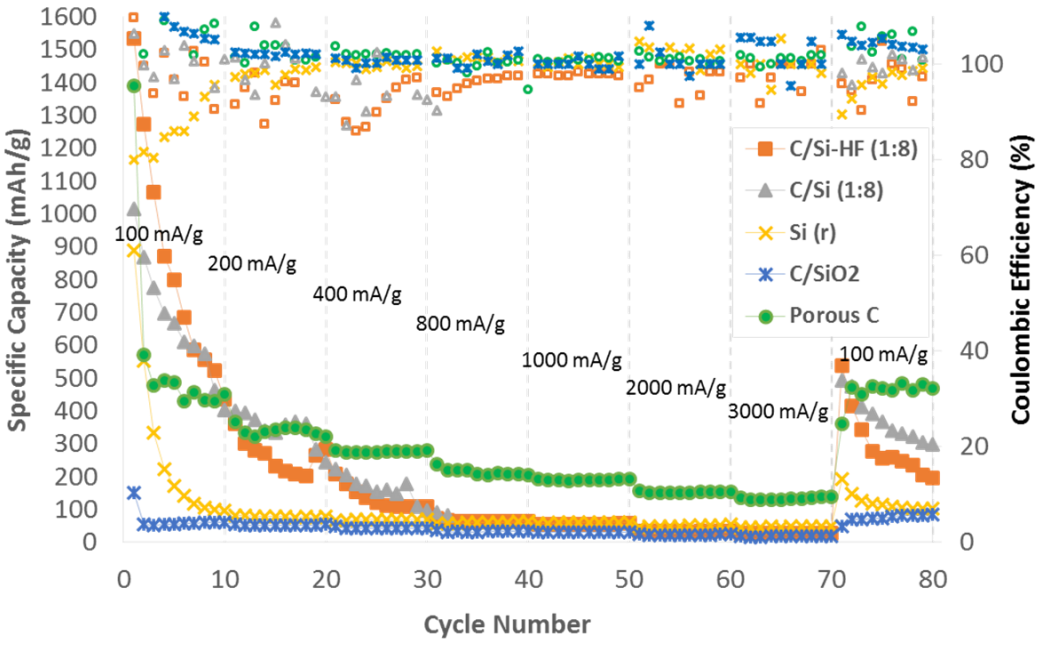

Figure 19. Rate capability of carbon spheres, C/SiO2, reduced C/SiO2 and reduced SiO2.

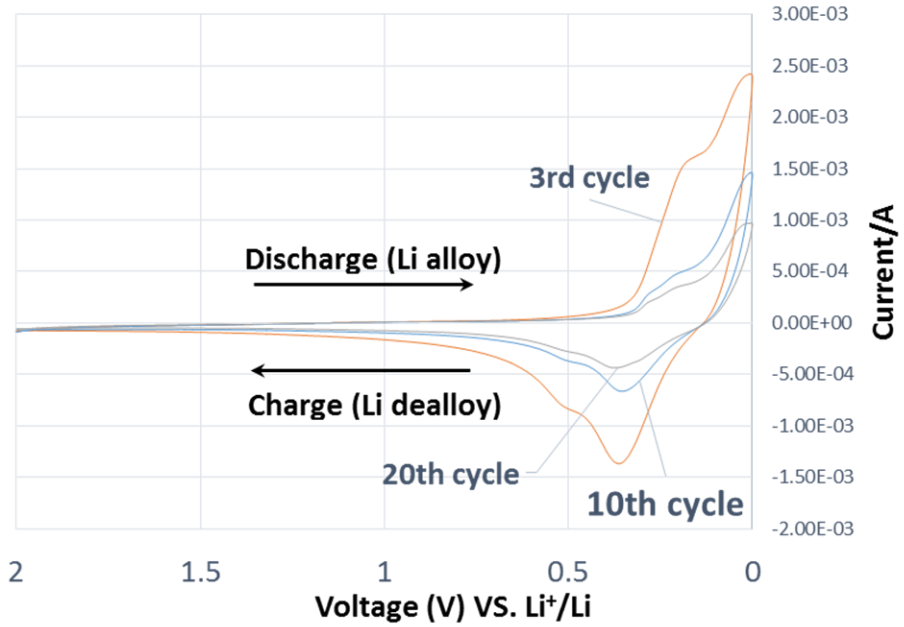

Figure 20. CV curves of the C/Si-HF (1:8) cycled under potential scanning between 2V and 0V.

SiO_2 (15-20 nm) reduced by magnesium (labeled as Si(r), Mg:Si = 2:1, 1.8:1 by atom) was tested as comparison to C/Si. The anode material use the reduced SiO_2 with a ratio of Mg:Si = 1.8:1, which resulted in a higher content of Si as shown in Figure 16. Note that this silica powder was different from the silica colloidal solution used in synthesizing C/Si, which used a Mg:Si ratio of 2:1. The initial specific capacity of Si(r) is 1073 mAh/g (see Figure 18), followed by a rapid drop at fixed C-rate. This demonstrated that the porous structure produced by magnesiothermic reduction alone is not enough to maintain a high capacity. The fast decrease of capacity is probably because the void space created by the removal of MgO (65% volume of the Si/MgO composite) is still not enough to accommodate a volume change of higher than 300%. With the large bulk structure, the Si material inside the bulk could not release the stress as freely as the surface, leading to destruction from within.

C/Si (1:2) showed a specific capacity near 100 mAh/g at 200 mA/g, much lower than PCMs. The reason is shown in XRD pattern in Figure 16. When the $C:SiO_2$ is 1:2 in weight, the product ratio C:Si is calculated to be about 1:1. However, most silicon reacted with carbon to form silicon carbide (SiC) during magnesiothermic reduction at 750 ℃. As a result, no silicon peak is shown in C/Si (1:2) sample. According to literature, silicon reacts with carbon at 800 ℃ for C_{60}[32]. However, this reaction temperature drops to 500 ℃ for amorphous carbon[33], which consists the carbon in this study. To create the silicon inside carbon spheres, a higher ratio of SiO_2 is needed to avoid depletion of Si during reduction. C/Si (1:5) and C/Si (1:8) were synthesized to verify the idea. From XRD pattern, the silicon amount in C/Si (1:5) was significantly

increased compared to C/Si (1:2), as expected. The specific capacity of C/Si (1:5) and C/Si (1:8) showed corresponding improvement during the first 50 cycles (see Figure 18) possibly to the increase of Si content. However, the capacity dropped to the same level as C/Si (1:2) after 50 cycles. Considering the sponge-like structure of the micron-sized spheres, the capacity loss might be caused by the fracture of Si frame, which was thin in diameter. In this case, the Si debris dissolved into the electrolyte and completely lost contact with the current collector.

To prove this hypothesis, the C/Si (1:5) and C/Si (1:8) samples were treated with sonication in 10% HF for five minutes. The products were labeled as C/Si-HF (1:5) and C/Si-HF (1:8). This process was supposed to remove some of Si and unreduced SiO_2, to create more void space in C/Si spheres. In the meanwhile, the Si structure became even thinner. The cycle performance of these washed samples is also shown in Figure 18. C/Si-HF (1:5) showed very similar capacity curve to C/Si (1:5). Possible reason could be the relatively low content of Si or a relatively more compact structure for HF to etch inside the spheres. C/Si-HF (1:8) showed obviously higher specific capacity (1532 mAh/g) than C/Si (1:8) (1015 mAh/g) due to the removal of surface SiO_2. However, the capacity of C/Si-HF (1:8) kept dropping more rapidly than C/Si (1:8) at current rates of 100 mA/g, 200 mA/g and 400 mA/g. In Figure 20, the CV curve also showed a very high dropping rate during cycling. The peaks on the discharging side indicated the lithiation reaction while the downward peak between 02-0.4V corresponded to the de-lithiation from silicon. The maximum current decreased by more than 40% from the 3rd cycle to the 10th cycle, suggesting poorer availability of the silicon participating in the

cycling. Based on the comparison between C/Si (1:8) and C/Si-HF (1:8), the decrease of reversibility and increase of initial capacity proved the hypothesis aforementioned, i.e., the thin structure of Si was vulnerable to volume change and caused the rapid decrease of specific capacity when the protecting carbon coating was destroyed. It's also worth mentioning that from Figure 19, the second cycle maintained 85% and 86% of the specific capacity from the initial cycle for C/Si (1:8) and C/Si-HF (1:8), respectively. This reversibility is much better than most silicon material reported in literature, and much higher than the porous carbon (41%). The high capacity of the second cycle also indicates the diameter of the frame network forming the "sponge" is proper for lithiation/de-lithiation, i.e., diffusion of lithium ions within the silicon.

6 CONCLUSIONS AND FUTURE WORK

In this study, failure mechanisms of porous C/Si material were investigated as anode material for Li-ion batteries. The C/Si material was achieved by magnesiothermic reduction of C/SiO_2 spheres, which were synthesized with carbonization of sucrose and spray-pyrolysis method. It's demonstrated that a highly porous Si is formed from magnesiothermic reduction of SiO_2 nanoparticles while the nanostructure is replaced with a continuous sponge-like structure with a channel size of 100 – 200 nm in diameter. With the addition of carbon to form C/SiO_2 spheres, the subsequent magnesiothermic reduction showed a preservation of spherical morphology while the inner porous structure was also maintained. Silicon carbide was formed at the high temperature and consumed part of the silicon reduced from silica. C/SiO_2 with low content ($C:SiO_2$=1:2) of SiO_2 was found to contain no Si after magnesiothermic reduction. C/Si (1:5) and C/Si (1:8) showed corresponding improvement due to the higher content of Si. When washed with 10% HF for five minutes, C/Si-HF (1:8) was found to have higher initial capacity but lower recovering efficiency than C/Si (1:8). This is caused by the removal of surface SiO_2 and Si, which lead to a thinner silicon frame. The thin Si structure was vulnerable to volume change without the protecting carbon sphere, which was destroyed during reduction.

Based on the results, silica has been successfully reduced to porous silicon with a pore/channel size and external size proper for lithium ion diffusion. The next step is to recreate the carbon coating to ensure high availability of the silicon (see Figure 21). This

is believed to improve the battery performance by providing better conductivity and preventing silicon debris from dissolving into electrolyte.

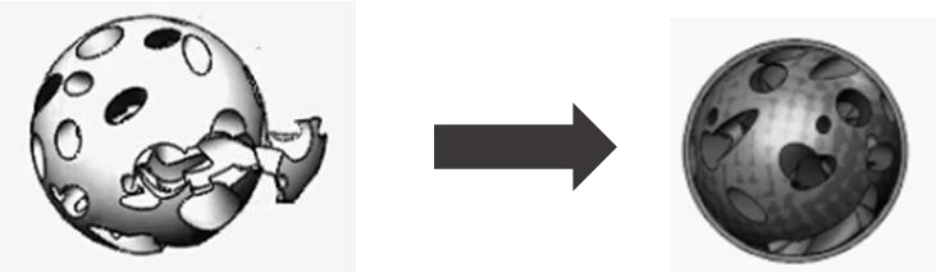

Figure 21. Carbon coating for debris protection.

Moreover, some stable forms of carbon such as C_{60}[32] and CNTs[34] have been reported to react with Si at much higher temperature (>800 ℃) than amorphous carbon (500 ℃) used in this study. One way to improve the carbon stability is to convert the amorphous carbon to graphite through high temperature annealing. The slilicon-graphite composite structure is supposed to be more strong and conductive, and be able to prevent the formation of SiC during magnesiothermic reduction at 750 ℃.

REFERENCES

1. Dunn, B., H. Kamath, and J.-M. Tarascon, *Electrical energy storage for the grid: a battery of choices.* Science, 2011. **334**(6058): p. 928-935.

2. Xu, K., *Electrolytes and Interphasial Chemistry in Li Ion Devices.* Energies, 2010. **3**(1): p. 135.

3. Obrovac, M. and L. Christensen, *Structural changes in silicon anodes during lithium insertion/extraction.* Electrochemical and Solid-State Letters, 2004. **7**(5): p. A93-A96.

4. Boukamp, B., G. Lesh, and R. Huggins, *All ‐solid lithium electrodes with mixed ‐conductor matrix.* Journal of the Electrochemical Society, 1981. **128**(4): p. 725-729.

5. Huggins, R.A., *Lithium alloy negative electrodes.* Journal of Power Sources, 1999. **81**: p. 13-19.

6. Wang, D., et al., *Self-assembled TiO2–graphene hybrid nanostructures for enhanced Li-ion insertion.* ACS nano, 2009. **3**(4): p. 907-914.

7. Yang, S., X. Feng, and K. Müllen, *Sandwich ‐Like, Graphene ‐Based Titania Nanosheets with High Surface Area for Fast Lithium Storage.* Advanced Materials, 2011. **23**(31): p. 3575-3579.

8. Wang, W., et al., *Monodisperse porous silicon spheres as anode materials for lithium ion batteries.* Scientific reports, 2015. **5**.

9. Ding, S., et al., *SnO 2 nanosheets grown on graphene sheets with enhanced lithium storage properties.* Chemical Communications, 2011. **47**(25): p. 7155-7157.

10. Chou, C.-Y. and G.S. Hwang, *On the origin of anisotropic lithiation in crystalline silicon over germanium: A first principles study.* Applied Surface Science, 2014. **323**: p. 78-81.

11. Kim, H., et al., *Novel hybrid Si film/carbon nanofibers as anode materials in lithium-ion batteries.* Journal of Materials Chemistry A, 2015. **3**(5): p. 1947-1952.

12. Ruffo, R., et al., *Impedance analysis of silicon nanowire lithium ion battery anodes.* The Journal of Physical Chemistry C, 2009. **113**(26): p. 11390-11398.

13. Vetter, J., et al., *Ageing mechanisms in lithium-ion batteries.* Journal of power sources, 2005. **147**(1): p. 269-281.

14. Bogart, T.D., et al., *Lithium ion battery peformance of silicon nanowires with carbon skin.* ACS nano, 2013. **8**(1): p. 915-922.

15. Chan, C.K., et al., *High-performance lithium battery anodes using silicon nanowires.* Nature nanotechnology, 2008. **3**(1): p. 31-35.

16. Cui, L.-F., et al., *Carbon− silicon core− shell nanowires as high capacity electrode for lithium ion batteries.* Nano Letters, 2009. **9**(9): p. 3370-3374.

17. Ge, M., et al., *Porous doped silicon nanowires for lithium ion battery anode with long cycle life.* Nano letters, 2012. **12**(5): p. 2318-2323.

18. Song, T., et al., *Arrays of sealed silicon nanotubes as anodes for lithium ion batteries.* Nano Letters, 2010. **10**(5): p. 1710-1716.

19. Peled, E., et al., *Tissue-like Silicon Nanowires-based 3D Anodes for High-Capacity Lithium Ion Batteries.* Nano letters, 2015.

20. Maranchi, J., A. Hepp, and P. Kumta, *High capacity, reversible silicon thin-film anodes for lithium-ion batteries.* Electrochemical and Solid-State Letters, 2003. **6**(9): p. A198-A201.

21. Chen, L., et al., *An amorphous Si thin film anode with high capacity and long cycling life for lithium ion batteries.* Journal of Applied Electrochemistry, 2009. **39**(8): p. 1157-1162.

22. Cui, L.-F., et al., *Light-weight free-standing carbon nanotube-silicon films for anodes of lithium ion batteries.* Acs Nano, 2010. **4**(7): p. 3671-3678.

23. Ng, S.H., et al., *Highly Reversible Lithium Storage in Spheroidal Carbon ‐Coated Silicon Nanocomposites as Anodes for Lithium ‐Ion Batteries.* Angewandte Chemie International Edition, 2006. **45**(41): p. 6896-6899.

24. Yao, Y., et al., *Interconnected silicon hollow nanospheres for lithium-ion battery anodes with long cycle life.* Nano Letters, 2011. **11**(7): p. 2949-2954.

25. Su, X., et al., *Silicon ‐based nanomaterials for lithium ‐ion batteries: a review.* Advanced Energy Materials, 2014. **4**(1).

26. Hu, R., et al., *Silicon/graphene based nanocomposite anode: large-scale production and stable high capacity for lithium ion batteries.* Journal of Materials Chemistry A, 2014. **2**(24): p. 9118-9125.

27. Liu, L., et al., *ZnO-CoO Nanoparticles Encapsulated in 3D Porous Carbon Microspheres for High-performance Lithium-Ion Battery Anodes.* Electrochimica Acta, 2014. **135**: p. 224-231.

28. Yin, Y.-X., et al., *Electrospray synthesis of silicon/carbon nanoporous microspheres as improved anode materials for lithium-ion batteries.* The Journal of Physical Chemistry C, 2011. **115**(29): p. 14148-14154.

29. Sourice, J., et al., *One-Step Synthesis of Si@ C Nanoparticles by Laser Pyrolysis: High-Capacity Anode Material for Lithium-Ion Batteries.* ACS applied materials & interfaces, 2015. **7**(12): p. 6637-6644.

30. Ming, J., J.-B. Park, and Y.-K. Sun, *Encapsulation of metal oxide nanocrystals into porous carbon with ultrahigh performances in lithium-ion battery.* ACS applied materials & interfaces, 2013. **5**(6): p. 2133-2136.

31. Magasinski, A., et al., *Toward efficient binders for Li-ion battery Si-based anodes: polyacrylic acid.* ACS applied materials & interfaces, 2010. **2**(11): p. 3004-3010.

32. Moro, L., et al., *Silicon carbide formation by annealing C60 films on silicon.* Journal of applied physics, 1997. **81**(9): p. 6141-6146.

33. Chung, C. and B. Wu. *Reaction of carbon and silicon at high temperature deposition*. in *Nano/Micro Engineered and Molecular Systems, 2008. NEMS 2008. 3rd IEEE International Conference on*. 2008. IEEE.

34. Sun, X.-H., et al., *Formation of silicon carbide nanotubes and nanowires via reaction of silicon (from disproportionation of silicon monoxide) with carbon nanotubes.* Journal of the American Chemical Society, 2002. **124**(48): p. 14464-14471.